Energy & Environmental Science

ROYAL SOCIETY OF CHEMISTRY

PAPER

View Article Online
View Journal | View Issue

Cite this: *Energy Environ. Sci.*, 2025, **18**, 9457

High-power hydrogel-based moisture-electric generators

Wenjun Ying,†[a] Zhoujun Huang,†[a] Zixiao Liu,†[b] Jinzhu Liu,[a] Nanzhe Pan,[a] Abdullatif Jazzar,[b] Jie Zhang,[a] Hua Zhang,[a] Ximin He, *[b] Ruzhu Wang *[c] and Jiayun Wang *[a]

Moisture-electric generators (MEGs) represent an emerging off-grid energy technology capable of generating electricity from ambient humidity; however, the power density and operational durability of existing MEG devices remain suboptimal, hindering their practical applications. Herein, we present a high-performance, highly flexible MEG achieved by integrating reduced graphene oxide (rGO) nanosheets and LiCl into a polyacrylamide (PAM) hydrogel matrix (namely PGL). The rGO nanosheets serve as conductive nanochannels that facilitate rapid ion transport and charge redistribution, synergizing with hygroscopic LiCl to boost output. By combining experiments, molecular-level simulations, and theoretical modeling, we establish rational and robust design principles for the intricate electricity generation process governed by chemical-mass transport-electric coupling, effectively guiding device design and enabling performance prediction. The resulting MEG unit achieves a superior open-circuit voltage of 0.6 V and a short-circuit current of 0.58 mA cm^{-2}, which previously required hundreds of MEGs connected in parallel. Notably, our MEG banks connected in series and in parallel are demonstrated to power wearable devices with integrated electronics. This work highlights a significant advancement in the design and scalability of MEGs, paving the way for their integration into flexible electronics and wearable technologies.

Received 5th August 2025,
Accepted 11th September 2025

DOI: 10.1039/d5ee04512f

rsc.li/ees

Broader context

Nowadays, with increasingly complex energy demands, such as self-powered wearable devices and flexible electronics, there is a growing need for power sources that not only generate electricity sustainably but are also flexible enough to adapt to complex application scenarios. The moisture-electric generator (MEG) harnesses electrical energy through the interaction of water molecules with functional materials, providing a promising solution to alleviate the power shortages in off-grid areas. Despite their promise, the development of high-performance MEGs remains challenging, particularly in achieving both operational stability and enhanced power output, owing to the lack of a comprehensive mechanistic understanding and reliable design rationale. This article proposes a hydrogel-based MEG device and verifies its power generation mechanism through experiments and molecular simulations. Multi-physics coupled numerical simulations predict the performance of MEGs and exhibit strong generality and can be readily extended to other hydrogel-based MEG systems. The resulting MEG unit achieves a superior open-circuit voltage of 0.6 V and a short-circuit current of 0.58 mA cm^{-2}, which previously required hundreds of MEGs connected in parallel. This work proposes a functional hydrogel design strategy for MEGs, which promotes their use in self-powered wearable devices and broadens the application possibilities.

Introduction

Nowadays, with increasingly complex energy demands, such as self-powered wearable devices[1] and flexible electronics,[2,3] there is a growing need for power sources that not only generate electricity sustainably but are also flexible enough to adapt to complex application scenarios. Conventional energy-harvesting systems, including solar cells and piezoelectric generators, face inherent limitations in deployment due to geographical constraints and intermittent energy supply.[4,5] Moisture-electric generators (MEGs) have emerged as a promising green

[a] *Institute of Refrigeration and Cryogenics, University of Shanghai for Science and Technology, 516 Jungong Road, Shanghai 200093, China. E-mail: jywang@usst.edu.cn*
[b] *Department of Materials Science and Engineering, University of California, Los Angeles, Los Angeles, CA, 90095, USA. E-mail: ximinhe@ucla.edu*
[c] *Institute of Refrigeration and Cryogenics, Shanghai Jiao Tong University, 800 Dongchuan Road, Shanghai 200240, China. E-mail: rzwang@sjtu.edu.cn*
† These authors contributed equally: Wenjun Ying, Zhoujun Huang, and Zixiao Liu.

alternative, capable of serving as a new off-grid energy source by harvesting ambient moisture—an abundant and ubiquitous, yet underutilized energy source—to generate electricity.[6,7] Their working mechanism relies on a complex interplay among water molecule adsorption on material surfaces, water diffusion within the material, and ion migration driven by concentration gradients and electric fields, which collectively convert chemical potential into electrical energy. Despite their promise, the development of high-performance MEGs remains challenging, particularly in achieving both operational stability and enhanced power output, owing to the lack of a comprehensive mechanistic understanding and reliable design rationale.[8,9]

Since the groundbreaking work by Qu *et al.*[10–12] in 2015, the MEGs have undergone significant advancements in voltage output and operational lifetime, driven by the development of novel nanomaterials and structural designs. In the early stage, MEGs fabricated from graphene oxide (GO) films[10] or graphene derivatives[13] produced intermittent energy output driven by fluctuations in external humidity. Subsequent studies have employed ionic functional groups or nanoporous materials such as proteins,[14] polymers,[15] biofibers,[16] and transition metal oxides/dihalides[17] to further enhance the hygroscopic capacity to facilitate water adsorption. Although these advancements have successfully increased the output voltage of MEGs from a few millivolts to nearly 1.5 V and extended the operational lifetime from seconds to hundreds of hours,[18–21] the practical application of most MEGs remains limited by their suboptimal current density, which remains below 10 μA cm^{-2}.[22,23] Such current levels are insufficient to visibly illuminate a standard LED, let alone power everyday portable electronic devices. In addition, many existing MEGs lack adequate stretchability and flexibility to adapt to changes in body curvature during daily activities, thereby limiting their applicability in wearable electronics.

Recent advancements in hydrogel-based MEGs have demonstrated that hydrogels could be a promising platform for next-generation MEG systems, owing to their unique properties.[24–26] The three-dimensional architecture of hydrogels offers exceptional hygroscopicity, attributed to their highly swellable matrix and abundance of functional groups, which facilitates rapid water adsorption to activate ion transport. However, one common challenge in hydrogel-based MEGs is that tightly cross-linked polymer chains formed through hydrogen bonding often restrict the mobility of free ions, resulting in limited ionic conductivity and mechanical flexibility, which intrinsically constrain the overall device performance. Fortunately, the remarkable tunability of hydrogels and their compatibility with a wide range of functional additives present opportunities to overcome these limitations. For instance, the stretchability can be effectively enhanced by designing a double network structure, and the ion transport properties can be enhanced by introducing chaotropic salt ions, such as lithium ions (Li^+), which disrupt hydrogen bonds between polymer chains according to the Hofmeister effect.[27–29] These strategies could further advance the development of high-performance hydrogel-based MEGs capable of addressing complex real-world application needs.

Another bottleneck for MEGs is the lack of a comprehensive understanding of the complex interplay among the material, water, and ions, as well as the absence of clear design principles. Consequently, MEG optimization still heavily relies on extensive experimentation and empirical knowledge. Previous studies have primarily focused on molecular-level mechanisms, employing molecular dynamics and first-principles calculations to elucidate material–water interactions,[30,31] such as the dissociation of functional groups on polyelectrolytes in moist environments. While these methods provide valuable insights into specific aspects of moisture-enabled energy conversion—such as the mechanism of ion generation—they do not directly bridge microscopic insights to macroscopic device performance. In practical terms, the electrical outputs of MEGs are governed not only by the generation of ions, but also by their subsequent migration and distribution, both of which are dynamically influenced by water and ion transport, concentration gradients, and the establishment of internal electric fields. The highly coupled nature makes the design space for MEGs exceedingly large. As a result, substantial performance variations can be observed even among nominally identical material systems.[1,32,33] Therefore, establishing a robust and comprehensive theoretical framework is urgently needed to predict humidity-driven power generation and guide rational MEG design strategies.

To address these issues, we designed a high-performance composite hydrogel, denoted as PGL. This material integrates a polyacrylamide (PAM) matrix, which provides a strong structural scaffold rich in amide groups. Reduced graphene oxide (rGO) nanosheets act as nanochannels, promoting rapid ion transport and efficient charge redistribution. The synergistic addition of lithium chloride (LiCl) imparts high hygroscopicity and invokes the Hofmeister effect, thereby weakening the interaction between the polymer and water and further promoting ion migration. The synergistic effect of these three components significantly enhances the power generation performance of the PGL hydrogel. Through a combination of experiments and molecular-level simulations, we elucidated the working mechanism of the MEGs. Notably, we developed a finite element model encompassing moisture adsorption, ion migration, and electrostatic field coupling to accurately predict the electrical output of MEGs, which exhibits strong generality and can be readily extended to other hydrogel-based MEG systems. Our PGL-based MEG unit (PMEG) can achieve an open-circuit voltage (V_{oc}) of 0.6 V and a superior short-circuit current (I_{sc}) of 0.58 mA cm^{-2} at 30 °C and 80% relative humidity (RH), which was typically achieved by hundreds of MEGs connected in parallel in the past. Our PMEG banks in series or in parallel can effectively power wearable electronic devices, including integrated devices such as smartwatches and e-ink screens. In summary, this work provides a new perspective on the design of a novel high-performance composite hydrogel with excellent environmental adaptability and provides new opportunities for energy supply in flexible electronics and self-powered wearable devices.

Results and discussion

Design principles and preparation of the PGL hydrogel

The basic operating principles of MEGs involve multiple coupled processes. First, the hydrogel directly adsorbs water molecules from the environment (Fig. 1A and B), which promotes the dissociation of numerous mobile protons from the hydrophilic groups on the hydrogel. Meanwhile, the negatively charged functional groups remain immobile due to their stronger bond to the structure of the hygroscopic material. By engineering a gradient conformation in the material[10,41] and utilizing asymmetric electrode deployment,[25,42] an ion gradient can be established within the hydrogel (Fig. 1C). This gradient drives the migration of mobile ions from regions of high to low concentration, generating an electrical signal that can be detected by the external circuit (Fig. 1D). The PGL design optimally leverages these mechanisms through three synergistic strategies to boost power output: increasing the material's moisture adsorption capacity, promoting ion dissociation, and enhancing ion conductivity.

Therefore, we developed a flexible electricity-generating material, comprising polyacrylamide (PAM), reduced graphene oxide (rGO) nanosheets, and lithium chloride (LiCl) *via* UV cross-linking and freeze-drying methods (detailed in Fig. S1). The specific design principles are as follows: (1) PAM serves as the matrix of the PAM-rGO-LiCl (PGL) hydrogel due to its three-dimensional, cross-linked hydrophilic network, in which the functional materials (such as salts and nanoparticles) can be introduced to further enhance moisture adsorption ability and ionic conductivity. Its amide groups (–$CONH_2$) can dissociate into fixed –$CONH^-$ and mobile H^+ in aqueous environments. Promoting directional H^+ transport is key to achieving a higher current output. (2) The rGO nanosheets can serve as conductive nanochannels, facilitating rapid ion transport and charge redistribution, while their high surface area and oxygen-containing functional groups enhance water adsorption and interfacial charge exchange, thereby modulating the resistance of the PGL hydrogel.[43] Meanwhile, the thermal reduction method helps adjust the mechanical properties and improves the stability of the PGL hydrogel.[44] (3) LiCl salt, which has strong hygroscopicity and low deliquescence RH (detailed in Fig. S2), was incorporated into the PAM-rGO aerogel to enhance water adsorption and promote ion dissociation and migration within the composite hydrogel. According to the Hofmeister effect, the dissociated chaotropic Li^+ ions disrupt hydrogen bonds between polymer chains, thereby widening ion migration nanochannels (Fig. 1E). Benefiting from our meticulous molecular design, the output voltage of the PMEG quickly rose to a maximum value of 0.6 V within 200 seconds in a controlled environment with constant temperature and humidity and 80% relative humidity (Fig. 1F). After about an hour and a half of moisture absorption, the I_{sc} signal slowly rose to a significant peak of 6.58 mA ($\sim$0.58 mA cm^{-2}) and then slowly decreased, which is more than ten times that of previously reported MEGs (Fig. 1G and Table S1).

Properties and characterization of the PGL hydrogel

The PGL hydrogel also exhibits remarkable stretchability and flexibility, which are of significant importance for the application of MEG devices. Fig. S3 presents the morphology of the final PGL hydrogel. By using homemade molds of different

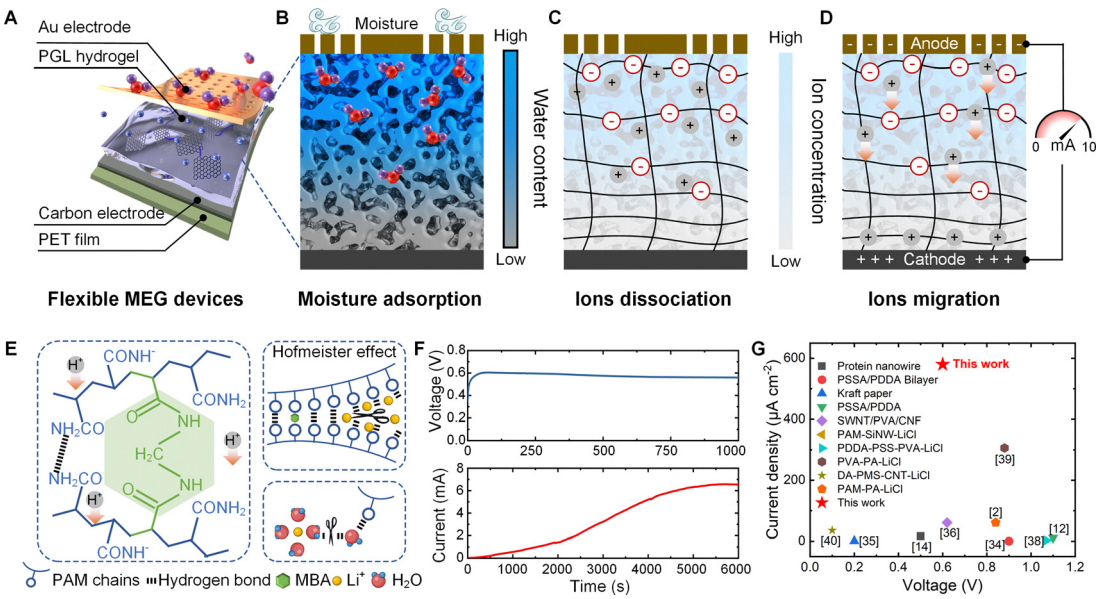

Fig. 1 Design of the PGL hydrogel for a high current density. (A) Schematic diagram of the flexible MEG devices. (B) Schematic diagram of the directional adsorption of water to form a water content gradient inside the gel. (C) The incoming moisture leads to the ionization of functional groups in the hydrogel, resulting in the release of ions. (D) Ions migrate directionally due to the ion concentration gradient. (E) The corresponding material composition and interactions that constitute the ionic hydrogel. (F) Open-circuit voltage and short-circuit current of the PMEG. Testing conditions: 80% RH, 30 °C. (G) Output performance comparison of the PMEG against prior MEGs.[2,12,14,34–40]

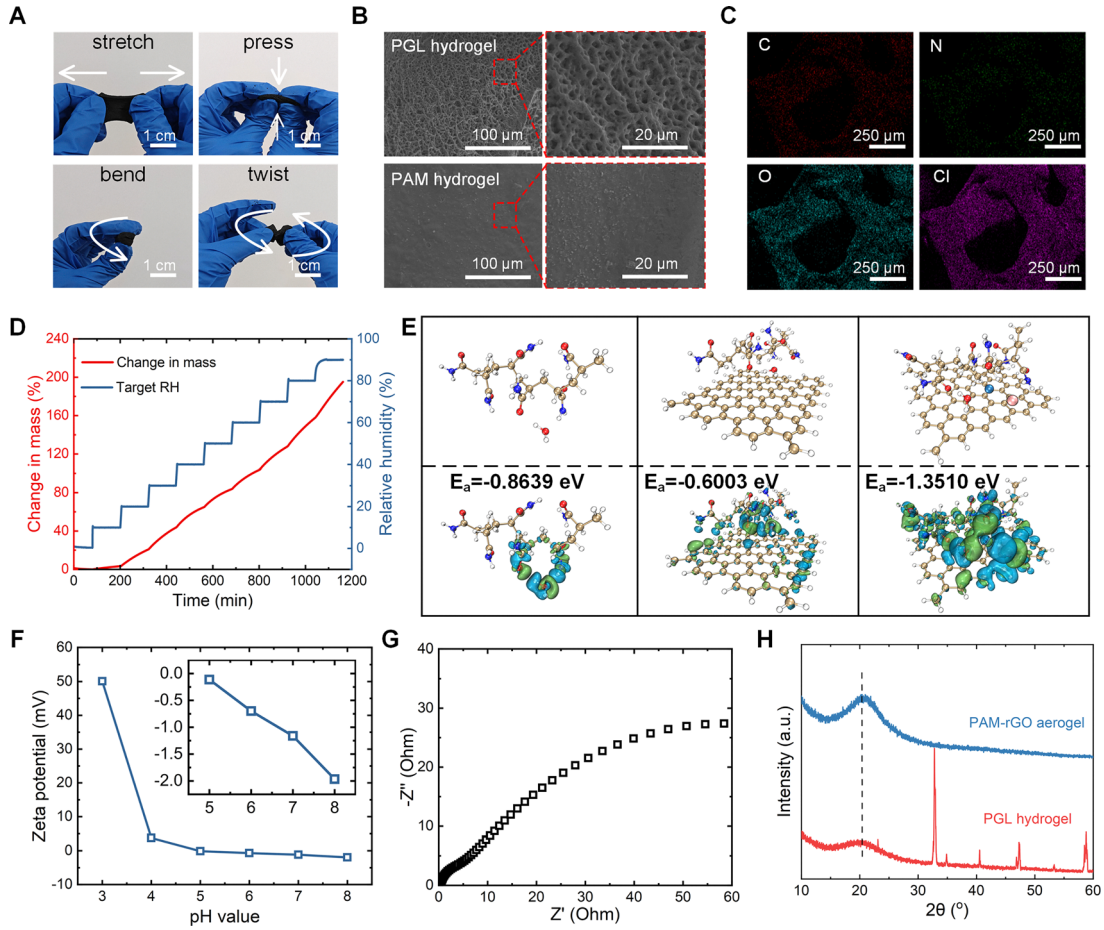

Fig. 2 Properties and characterization of the PGL hydrogel. (A) The reliable mechanical properties of the PGL hydrogel. (B) Comparison of scanning electron microscopy (SEM) images between the gel treated with freeze drying and thermal reduction treatment and untreated gel. (C) Energy dispersive spectroscopy (EDS) results of the PGL hydrogel. (D) Moisture adsorption kinetics of the PGL hydrogel at 25 °C. (E) CDD simulations of PAM-H_2O, PAM-rGO-H_2O, and PAM-rGO-LiCl-H_2O systems, respectively, from the left to the right. (F) The zeta potential of the PGL hydrogel in the pH range of 3 to 8. (G) The electrochemical impedance spectroscopy (EIS) results of the PGL hydrogel after adding LiCl. (H) XRD patterns of hydrogels with and without LiCl.

sizes, shapes, and dimensions, PGL hydrogels with varying geometries can be easily tailored. As shown in Fig. 2A, under substantial stretching, pressing, bending, and twisting, the PGL hydrogel retains its original shape without cracking or irreversible deformation. Moreover, the PGL hydrogel can be easily stretched to a strain of 126%, corresponding to an ultimate tensile stress of 20 MPa, making it two thousand times stronger than a pure PAM hydrogel without the UV cross-linking process (Fig. S4). During compression testing, the PGL hydrogel also maintained its structural integrity under a compressive strain of up to −90%, enduring a peak stress of −0.9 MPa, which also surpasses the performance of the pure PAM hydrogel (Fig. S5).

Fig. 2B illustrates the microscopic morphology of the material obtained using SEM. The pure PAM hydrogel, without undergoing free-drying and GO thermal reduction, is dense and has no large pores. In contrast, the PGL hydrogel has a richer internal pore structure, with pore sizes ranging from a few microns to more than microns. This proves that our preparation process can provide hydrogels with abundant pores for water adsorption. EDS analysis confirmed that LiCl was successfully incorporated into the PAM-rGO aerogel and is uniformly distributed throughout the polymer matrix after the salt impregnation (Fig. 2C). The X-ray photoelectron spectroscopy results in Fig. S6 also confirm the addition of LiCl. Benefiting from the strong hygroscopicity of LiCl, as shown in Fig. 2D, the PGL hydrogel exhibits strong water molecule adsorption ability at all relative humidity levels. To further substantiate the role of LiCl in enhancing moisture absorption, charge density difference (CDD) calculations were performed using density functional theory (DFT) and the Multiwfn code.[45] As shown in Fig. 2E, an isosurface value of 0.001 eV was employed, with blue and green regions representing electron density depletion and accumulation, respectively. The calculated adsorption energy of water molecules on the surface of the PGL material was −1.351 eV, significantly lower than that of the original PAM-rGO aerogel, which was −0.6003 eV (detailed in Note S1 and Table S2). These findings illustrate that lithium chloride plays a crucial role in the adsorption of water molecules by PGL hydrogels.

Zeta potential measurements were conducted across a pH range from 3 to 8 to assess ion dissociation. As illustrated in Fig. 2F, the zeta potential of the PGL hydrogel at a pH value of 7

was −1.1 mV, indicating a negative surface charge. This negative charge is largely due to the high concentration of amide groups associated with the polymer chains following the dissociation of free hydrogen ions (H^+). To visually demonstrate the processes of water diffusion and ion migration, the PGL hydrogel was placed in a beaker containing an isopropanol solution of the bromophenol blue pH indicator, as illustrated in Fig. S7. Upon the addition of liquid water, the color of the solution changed from blue to yellow, confirming that the PGL hydrogel released hydrogen ions, which caused an increase in the pH value.

To compare the mobility of ions, the ionic conductivities of the PGL hydrogel (Fig. 2G) and the PAM-rGO aerogel (Fig. S8) were measured using electrochemical impedance spectroscopy fitted to equivalent circuits. The fitting results indicate that the PGL hydrogel containing lithium ions (Li^+) exhibits a relatively high ionic conductivity of 4.69 S m^{-1}, substantially greater than that of the PAM-rGO aerogel without Li^+. Furthermore, the ionic conductivity of PGL hydrogels surpasses that of conventional ionic hydrogels, typically around 1 S m^{-1}, highlighting that the increased ionic conductivity can be attributed to the presence of Li^+. X-ray diffraction (XRD) was employed to investigate Li^+-induced structural modifications. As shown in Fig. 2H, while the PAM-rGO aerogel maintains a characteristic peak at 20° (attributed to ordered PAM polymer chains), this peak intensity is markedly reduced in the PGL hydrogel. We then performed FTIR measurements on the PGL hydrogel and the PAM-rGO aerogel (Fig. S9). Upon LiCl addition, the N–H asymmetric and symmetric stretching vibrations at 3340 cm^{-1} and 3186 cm^{-1} exhibited significant blue shifts of 30 cm^{-1} and 95 cm^{-1}, respectively. Concurrently, the N–H bending vibration at 1600 cm^{-1} is also blue-shifted by approximately 30 cm^{-1}. These shifts arise from the rupture of hydrogen bonds that previously elongated the N–H bonds and induced red-shifted vibrations. We further utilized MD simulations to generate trajectories to quantify the number and length distribution of interchain hydrogen bonds in the PAM matrix during LiCl immersion (the simulation method is described in Note S2). As shown in Fig. S10A, in the absence of LiCl, the mean inter-chain hydrogen-bond count was 882.25. In contrast, upon incorporation of 5 wt%, 10 wt%, 20 wt%, and 40 wt% LiCl, the values decreased to 654.23, 630.42, 650.92, and 637.35, respectively. This marked reduction demonstrates that LiCl absorption disrupts the hydrogen-bond network between PAM chains, consistent with the weakening of intermolecular interactions. Notably, the pronounced decrease in strong hydrogen bonds created more favorable diffusion pathways for ions, while LiCl did not significantly alter the intrinsic hydrogen-bond length—the dominant peak remained near ∼0.29 nm (Fig. S10B). These structural changes demonstrate how Li^+ ions, through the Hofmeister effect, competitively break polymer–polymer hydrogen bonds and promote chain separation.

Moisture-electric generation performance of the PMEG

To optimize the electrical performance of the PMEG, the UV irradiation time and salt loading during the preparation of PGL hydrogels were further quantitatively investigated. The UV irradiation accelerates the polymerization process, enabling precise control over the degree of polymerization by adjusting the irradiation time. Generally, longer UV irradiation times lead to more complete polymerization, resulting in a denser internal structure of the hydrogel. Moisture adsorption curves of PGL hydrogels prepared under varying UV irradiation durations were measured (Fig. S11). It was observed that the moisture adsorption capacity decreased as the UV irradiation time increased. This reduction may be attributed to the excessively dense internal structure of the PGL hydrogel, which reduces the surface area available for moisture adsorption. Subsequently, the electrical output of the devices was assessed, revealing that the PMEG containing the PGL hydrogel exposed to UV irradiation for 20 minutes exhibited the best performance in both voltage and current output (Fig. 3A). From these findings, it can be concluded that the hygroscopicity of the PGL hydrogel significantly impacts the electrical properties of the PMEG, establishing 20 minutes as the optimal UV irradiation duration for enhancing performance.

The influence of hygroscopic salts on the performance of the PGL hydrogels was subsequently investigated. PAM-rGO aerogels were impregnated with solutions of five common hygroscopic salts to fabricate the corresponding composite materials. Among these, LiCl yielded the strongest electrical output (Fig. S12), which is attributed to its exceptional hygroscopic capacity and its efficacy in promoting ion mobility *via* the Hofmeister effect. Subsequently, the concentration of the LiCl solution was optimized. As shown in Fig. 3B, as the LiCl content increased from 5 wt% to 40 wt%, the electrical output of the PMEG first increased to a peak value at an intermediate content of ∼10 wt% and then decreased at higher concentrations. Dynamic moisture adsorption tests revealed a similar trend relative to the LiCl concentration (Fig. S13). At low LiCl concentrations, the hydrophilic capacity of the material was insufficient to facilitate the mobility of ions necessary for efficient ion migration.[46] Conversely, at concentrations exceeding 10%, while the moisture adsorption capacity increased, the accumulation of salts within the pore nanochannels hindered ion transport and slowed down the kinetics of moisture adsorption. Molecular dynamics simulations were conducted using GROMACS software to investigate the adsorption kinetics by analyzing the mean square displacement of internal molecules (see Note S2 and Fig. S14). The simulation results in Fig. S15 also indicate that the adsorption kinetics reached their optimum at a LiCl concentration of 10 wt%. Moreover, the introduction of LiCl significantly improved the ionic conductivity of the device, which led to a much higher output current than devices without LiCl (Fig. S16).

The geometry of the PGL hydrogel also plays a key role in PMEG's electrical output performance. Specifically, the thickness of the hydrogel influences the ion concentration gradient and the diffusion distance, which are vital factors in ion mobility and electrical output (Fig. S17).[47] When the PGL hydrogel was too thin, the gradient in ion concentration was rather small, and the output was restricted. Conversely, when

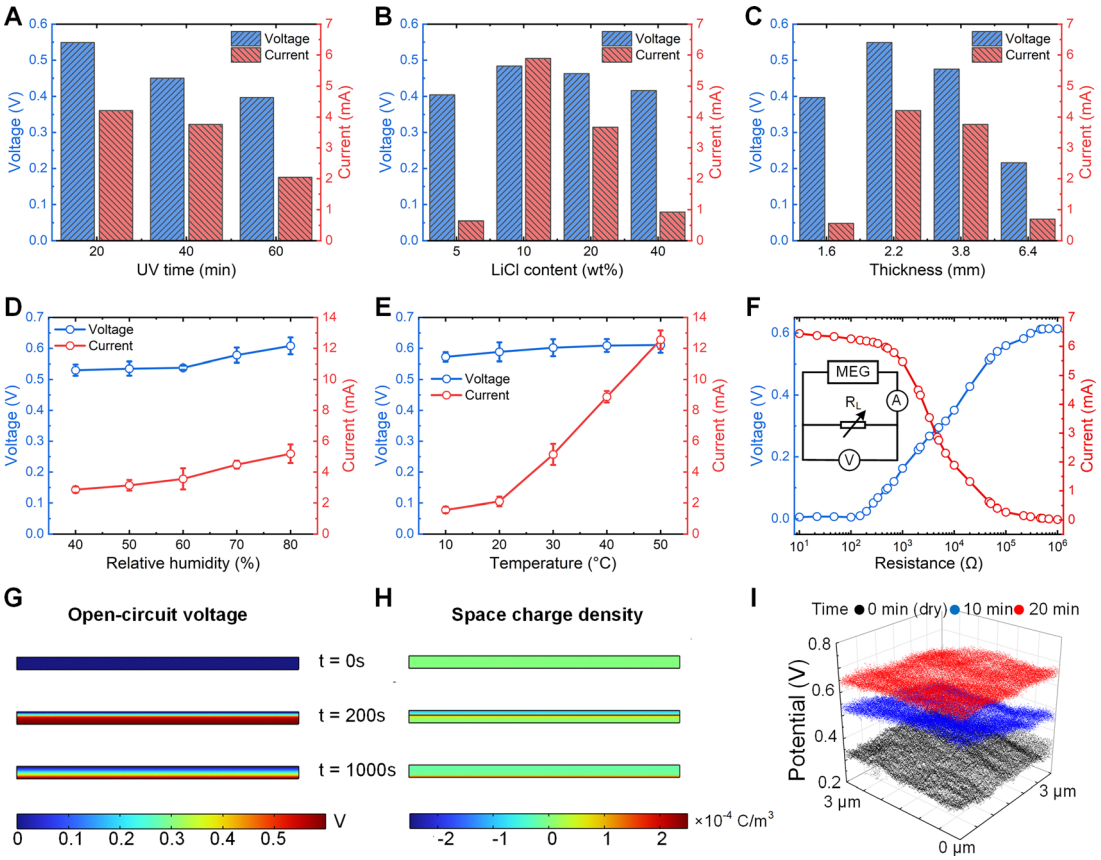

Fig. 3 Electric generation of a PMEG unit. The voltage and current of the PMEG are based on PGL hydrogels with variations in (A) UV time, (B) salinity, and (C) thickness under conditions of 30 °C and 80% RH. (D) The variation of stable V_{oc} and I_{sc} *versus* RH change at 30 °C. (E) The variation of stable V_{oc} and I_{sc} *versus* temperature change at the relative humidity of 80% RH. (F) The electric output of the PMEG with external resistance varied from 10^1 to 10^6 Ω at 30 °C and 80% RH. (G) Simulation of space charge density variation of the PMEG. (H) Simulation of open-circuit voltage variation of the PMEG. (I) Potential changes on the non-wetting side of the PGL hydrogel were obtained from the KPFM test.

the PGL hydrogel was too thick, the diffusion pathway for ions and water molecules in the interior nanochannels was too long, slowing the ionic diffusion to the bottom electrode. The optimal thickness of the PGL hydrogel was found to be ~2.2 mm (Fig. 3C). Furthermore, the electrical output of the PMEG can be effectively tuned by adjusting the device area because the larger the surface area of the PGL hydrogel, the stronger its water adsorption capacity. This, in turn, allows the release and migration of more ions, resulting in a higher current output (Fig. S18).

In practical applications, the environmental adaptability of the device is crucial. To assess this, we compared the performance of the PMEG under various operating conditions. The power-generating performance of most MEGs significantly decreases in low-humidity environments due to insufficient interaction between water molecules and the power-generating materials. As shown in Fig. S19 and S20, the electrical outputs of many previously reported MEGs weaken considerably under arid conditions (approximately 40% RH), with some cases seeing the output current drop to zero, which restricts their applicability across diverse environments.[34,41,47–51] In contrast, Fig. 3D illustrates that our PMEG can maintain a relatively high electrical signal output regardless of whether the environment is humid or dry, which is due to the high moisture absorption ability of LiCl in a wide humidity range. Remarkably, even at a low humidity level of 40% RH, the short-circuit current (I_{sc}) of the PMEG remains substantial at 3 mA, corresponding to a current density of approximately 0.24 mA cm^{-2}, which is hundreds of times higher than that of other MEGs (refer to Fig. S20). This indicates a strong power capability in arid environments. Temperature also plays a critical role in performance, and the PMEG has shown competitive performance under a range of temperatures. As illustrated in Fig. 3E, the I_{sc} increases from 20 °C to 40 °C, reaching a peak value of 8.89 mA. This trend can be attributed to improved adsorption kinetics and enhanced ion diffusion across different environmental conditions (see Fig. S21). Both increased temperature and humidity elevate the partial pressure of water vapor, facilitating moisture adsorption by hygroscopic materials and promoting the subsequent release and migration of ions, further enhancing performance. In summary, the PMEG reliably maintains excellent electrical output performance across a wide range of humidity and temperature conditions, underscoring its potential for practical applications.

In addition to the properties of the PGL hydrogel itself, the power generation performance is also related to the electrodes and external resistance. Cyclic voltammetry was first used to analyze the effects of the electrodes. The curves exhibited a

nearly rectangular shape at scan rates from 0 to 100 mV s^{-1}, which is characteristic of capacitive behavior and confirms the absence of redox reactions at the electrode (Fig. S22). Subsequently, the critical role of electrode asymmetry was evaluated by comparing the asymmetric (Au–C) electrode pair against symmetric control configurations (Au–Au and C–C). The output current and voltage generated by the symmetric structures were significantly lower than those of the asymmetric design (Fig. S23), unequivocally demonstrating that electrode asymmetry is essential for optimizing electrical output. Finally, the performance of the PMEG as a power supply was further analyzed, particularly examining the dependence of voltage and current on the resistance of the external circuit (Fig. 3F). As the resistance increased from 10 Ω to 1 MΩ, the PMEG voltage gradually increased, while the current gradually decreased. A maximum power output of 1 mW was achieved at approximately 2 kΩ (Fig. S24).

Theoretical framework of the PMEG

Based on the above analysis, we found that the electricity generation in the MEG device results from the synergistic interplay of several physical and chemical processes, including water adsorption and diffusion, functional group dissociation, H^+ transport, and electric field formation. At the open upper boundary of the device, the adsorbent material surface continuously captures water molecules from the ambient environment. The diffusion behavior of the adsorbed water within the hydrogel is governed by eqn (1). Concurrently, increasing water content induces the dissociation of hydrogen ions from the functional groups. These dissociated protons not only diffuse due to concentration gradients but also migrate in response to potential variations. To model the mass and charge transfer of hydrogen ions, we employ the Nernst–Planck equation [eqn (2)]. Additionally, to accurately describe the system, the influence of ion concentration changes on the electric potential ϕ must be accounted for *via* the Poisson equation [eqn (3)]. The coupled governing equations form the theoretical foundation of our model. Further details regarding boundary conditions and the complete modeling procedure are provided in Note S3.

$$\frac{\partial C_w}{\partial t} - \nabla \cdot (D_w \nabla C_w) = 0 \quad (1)$$

$$\frac{\partial C_{H^+}}{\partial t} + \nabla \cdot \left(-D_{H^+} \nabla C_{H^+} - \frac{D_{H^+} z_{H^+} F}{RT} \right) = R_{H^+} \quad (2)$$

$$\nabla^2 \phi = \frac{\rho}{\varepsilon} \quad (3)$$

where C_w denotes the water content, D_w is the diffusion coefficient of water in the hydrogel, C_H denotes the H^+ concentration, and D_H is the diffusion coefficient of H^+ ions. z_H is the valence (with a value of +1 for H^+), R is the universal gas constant, T is the temperature, F is the Faraday constant, ε is the permittivity, and ρ is the charge density.

Fig. 3G and H present the simulated spatiotemporal evolution of voltage and space charge density (defined by the local difference between H^+ and $CONH^-$ concentrations, detailed in Fig. S25) for 1000 s, respectively. The results demonstrate that the dissociation and subsequent migration of hydrogen ions, combined with the fixation of $CONH^-$, lead to a progressive accumulation of space charge density, thereby establishing an intrinsic potential difference. This result can be verified by Kelvin probe force microscopy (KPFM) to investigate potential changes on the nonwetting side of the PGL hydrogel, as the other side was exposed to atmospheric humidity (Fig. S26). As illustrated in Fig. 3I, water-induced ion diffusion increased the potential of the nonwetting side of the PGL hydrogel by ~450 mV after twenty minutes of moisture uptake, which is consistent with the results of numerical simulation. This suggests that a water gradient triggers ion transport behavior. Importantly, when the hygroscopic sample was subsequently dried, the surface potential returned to its initial value, indicating that the changes in hydrogel surface potential were reversible.

The voltage change caused by the space charge density is shown in Fig. S27A. Although hydrogen ions continue to migrate, the voltage reaches its maximum value at approximately 200 s, after which it gradually decays due to the diminishing concentration gradient. This trend shows excellent agreement with the experimental data, validating our numerical model. Furthermore, as shown in Fig. S27B–D, additional simulations investigating the effects of UV exposure duration (affecting the cross-linking degree of the material), LiCl concentration (affecting the moisture absorption and diffusion capacity), and relative humidity (affecting the boundary condition for moisture adsorption) all yielded results that were consistent with experimental observations. This comprehensive agreement between simulation and experiment strongly supports that our numerical model can accurately predict the performance of the PMEG and provide effective guidance for the material preparation process.

Integrated PMEGs for practical applications

The scalability, sustainability, and flexibility of PGL hydrogels provide a solid foundation for integrating PMEG devices in self-powered wearable electronic devices, as shown in Fig. 4A. In practical applications, the electrical output of the PMEG can be amplified by connecting multiple devices either in series or in parallel. As illustrated in Fig. 4B, the voltage output of the PMEG increases almost linearly with the number of devices connected in series, while the current output increases similarly with parallel connections. Generally, by connecting three PMEGs in series, it is possible to easily achieve a voltage of 1.5 V, comparable to that of a common dry cell. Additionally, due to the high current density of PMEGs, a 6 cm^2 unit can generate an I_{sc} of 2 mA, surpassing the output of tens or even hundreds of other MEGs when connected in parallel.[23,28] By increasing the size of the PMEG or the number of parallel connections, the current output of a single PMEG can be further enhanced, allowing for customized designs to meet specific power requirements.

To demonstrate the sustainability and environmental adaptability of the PMEG, its power output was recorded over an extended period under natural conditions. In outdoor tests

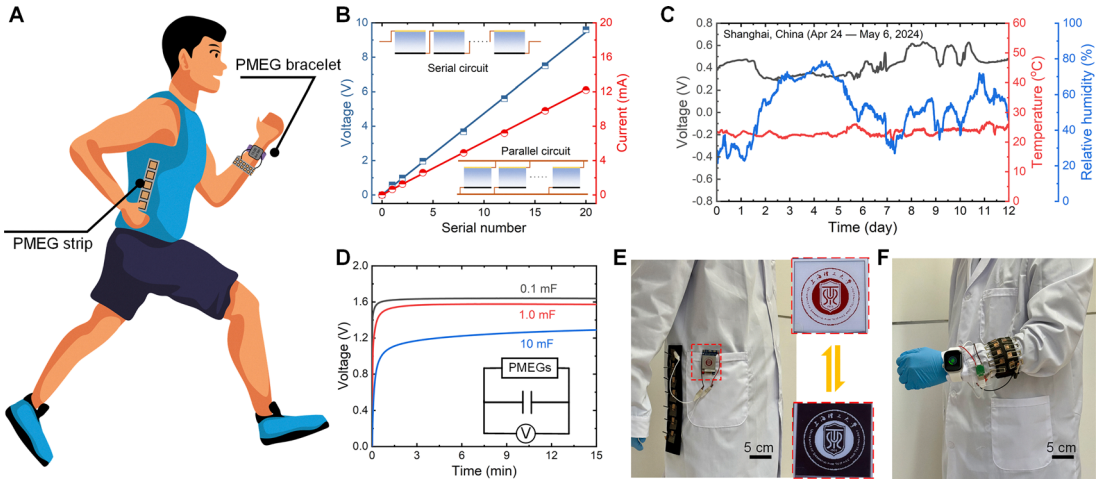

Fig. 4 Integration and applications of the PMEG. (A) Schematic of high-performance self-powered wearable PMEGs driving self-powered wearables and flexible electronics. (B) The V_{oc} and I_{sc} of PMEGs with different serial and parallel numbers, respectively. The insets show the serial and parallel circuits. (C) Voltage variation generated by a PMEG during outdoor testing. (D) Voltage–time curves of commercial capacitors with various capacitances (0.1, 1, and 10 mF) charged by the integrated PMEGs. (E) Photograph of a coat integrated with a 7 × 1 PMEG bank charging an ink screen. (F) Photograph of a ring-shaped wristband integrated with a 6 × 4 PMEG bank charging a smartwatch.

conducted in Shanghai, the voltage output of the PMEG fluctuated between 0.4 V and 0.6 V under environmental conditions of approximately 30–80% RH and temperatures ranging from 20 to 30 °C over 12 days (Fig. 4C). Furthermore, the electrical output of the PMEG remained stable over more than 40 adsorption–desorption cycles, demonstrating the stability of its internal structure and performance (Fig. S28). Quantitative analysis of the Li^+ concentration in samples before and after the experiment using inductively coupled plasma optical emission spectrometry (ICP-OES) revealed no significant change in Li^+ content before and after the cycles, confirming the absence of salt deposition or leakage (Fig. S29). Moreover, the power generated by the PMEG could be stored in commercial energy-storage devices without additional rectifiers and power management circuitry. As shown in Fig. 4D, a capacitor of 0.1 mF or 1 mF was charged to 1.6 V within 100 s, and even a capacitor of 10 mF could be charged to 1.2 V within 10 min by five units connected in series. This contrasts sharply with previously reported integrated MEGs, which typically require several hours to charge a 1000 μF capacitor.[36]

In practical applications, we evaluated the ability of PMEG groups to power portable electronic devices. As demonstrated in Fig. 4E, a PMEG strip composed of seven 6 cm^2 units connected in series can continuously power an ink screen. Additionally, the reliable flexibility of the PMEG expands its potential applications in wearable self-powered devices. As shown in Fig. S30, the PMEG maintains a stable voltage output even when subjected to varying degrees of bending. To illustrate this, we designed a power bracelet that incorporates 1.5 cm^2 PMEG units connected in a series–parallel configuration (6 × 4), which comfortably fits the wrist of an adult male and can effectively power a smartwatch (Fig. 4F). With the help of capacitors, it is also feasible to power larger electrical appliances. Fig. S31 illustrates a 16-unit PMEG bank charging a mobile phone. These practical applications highlight the versatility, high power density, and scalability of the PMEG. Notably, our PMEG devices demonstrate significant cost-effectiveness, with a material and fabrication cost of approximately $35.6 per square meter (detailed in Table S3). These results position the PMEG as a promising sustainable energy solution for diverse IoT applications.

Conclusion

In summary, we developed a high-performance, mechanically robust, and flexible PMEG based on functional composite PAM-rGO-LiCl hydrogels. We validate the working mechanism through experiments and molecular simulations and propose a general numerical model that couples moisture absorption, ion diffusion, and electrostatic fields to accurately predict the performance of the PMEG and guide optimal design. As a result, one PMEG unit can produce a V_{oc} of around 0.6 V and an impressive I_{sc} of up to 580 μA cm^{-2} at 30 °C and 80% relative humidity. Additionally, the PMEG maintains a consistent voltage output of approximately 0.6 V across a wide temperature range (10–40 °C) and varying humidity levels (30–100%), showcasing exceptional environmental adaptability. Furthermore, the series and parallel MEG groups linearly amplify voltage and current signals, respectively, enabling their integration into wearable devices like smartwatches and ink screens to power them, exhibiting the potential for application in self-powered wearable devices. This work proposes a functional hydrogel design strategy for MEGs, which promotes their use in self-powered wearable devices and broadens the application possibilities.

Experimental section

Synthesis of GO

Graphite oxide (GO) was prepared from the oxidation of natural graphite powder using a modified Hummers' method. In brief,

1 g of graphite powder and 0.5 g of sodium nitrate were mixed, followed by the addition of 23 mL of concentrated sulfuric acid under constant stirring under the condition of an ice water bath. After 1 h, 3 g of $KMnO_4$ was slowly added to the mixed solution while keeping the temperature under 20 °C to prevent overheating and explosion. After stirring at 35 °C for 12 h, the resulting solution was diluted by adding 500 mL of deionized water under vigorous stirring. The suspension was further treated with a 30% H_2O_2 solution (5 mL) to ensure the completion of the reaction with $KMnO_4$. The resulting mixture was washed with HCl and deionized water, respectively, followed by filtration and drying; the final product GO was thus obtained.

Preparation of the flexible PGL hydrogel

The flexible PGL hydrogel was synthesized through free radical polymerization and solvent displacement. Typically, 1 g of acrylamide (AM) was added to 10 mL GO suspensions in water (2.5 mg mL^{-1}) under stirring to form the monomer solution. Then, 1 mg of *N*,*N*′-methylenebisacrylamide (MBA, as a crosslinker) was added to the above solution under stirring for a certain time (10 minutes) until a homogeneous solution was obtained. Finally, ammonium persulfate (APS, as an initiator) and *N*,*N*,*N*′,*N*′-tetramethylethylenediamine (TEMED, as a catalytic agent) were added under stirring. After stirring for 5 minutes, the mixed solution was poured into the desired mold and exposed to UV light (40 W, 365 nm) for a certain period (*e.g.*, 20 minutes) to accelerate the cross-linking polymerization process. Next, the crosslinked products were freeze-dried for 24 hours to obtain the unreduced PGL aerogel. The GO component was further reduced into rGO through thermal reduction in a vacuum oven for 2 h at 160 °C. The reduced aerogel was immersed in a 10 wt% aqueous LiCl solution for 24 h to achieve the salt-loading process. After the salt immersion step, the hydrogel was dried in an oven at 70 °C for 12 h to obtain the final PGL hydrogel. To study the effect of LiCl concentration on the ionic conductivities of the hydrogels and electrical output performance of the MEG, the contents of LiCl were varied from 5, 10, 20, to 40 wt%.

Fabrication of the PMEG

The PGL hydrogel was used as an electricity-generating material. The top electrode was made of stainless-steel mesh with gold sputtering treatment. The stainless-steel mesh is 16 mesh with a thickness of 0.8 mm and a size of 5 × 5 cm. Commercial graphite sheets without holes were directly used as bottom electrodes. The PGL hydrogel was sandwiched between stainless-steel/graphite electrodes, and a PMEG device was simply obtained.

Characterization

The morphology of the PGL hydrogel was observed by scanning electron microscopy (SEM, JSM-IT500HR, JEOL, Japan). The chemical structure and mechanical properties of the hydrogel were characterized by Fourier transform infrared spectroscopy (FTIR, Nicolet IS50, Thermo Fisher Scientific, USA). X-ray photoelectron spectroscopy (XPS) measurements were performed on an ESCALAB 250XI photoelectron spectrometer (Thermo Fisher Scientific, USA) with an Al Kα source. The weight and thickness of the prepared samples were tested with an electronic balance (PRACTUM224-1CN, Sartorius Ltd, Germany) and a thickness gauge (Syntek, Deqing Shengtaixin Electronic Technology Co., Ltd, China). The electrochemical impedance spectroscopy (EIS) measurements were taken on a CHα 660E electrochemical workstation (Shanghai Chenhua Instrument Co., Ltd, China). Energy dispersive spectroscopy was performed using a scanning electron microscopy system (JSM-IT500HR, JEOL, Japan). The temperature and degree of humidity in the atmosphere were recorded with a temperature and humidity transmitter (HCTR-HTS21D4XX, Widron Measurement and Control Co., Ltd, China).

Electric measurements

All the voltage and current signals were recorded in real-time using a Keithley 2601B source meter (Keithley Instruments, Inc., USA), which was controlled by a data acquisition software called KickStart. The circuit parameter of the open-circuit voltage test was set to 0 nA. The circuit parameter of the short-circuit parameter test was a voltage of 0 mV. All the samples were short-circuited before testing to avoid any interference from static electricity. Testing conditions (temperature and humidity) are controlled by a constant temperature and humidity chamber (Fig. S32).

Author contributions

W. Y. and Z. H. designed the experiment and fabricated the device. W. Y. and Z. L. wrote the manuscript. Z. L. and A. J. revised the manuscript. J. L. and Z. H. conducted the electrical output measurements. N. P. and J. Z. performed the MD and DFT calculations. Z. L. performed the FEM calculations. R. W. H. Z. and X. H. advised the project and reviewed the manuscript. J. W. guided the project and supervised the work. All authors read and approved the manuscript.

Conflicts of interest

The authors declare no competing interests.

Data availability

All data associated with the study are included in the article and the supplementary information (SI). Supplementary information is available. See DOI: **https://doi.org/10.1039/d5ee04512f**.

Additional information is available from the corresponding authors upon reasonable request.

Acknowledgements

The authors gratefully acknowledge the support and funding for this research sponsored by the General Program of the

National Natural Science Foundation of China (No. 52376203) and the Foundation for Innovative Research Groups of the National Natural Science Foundation of China (Grant No. 51521004). The authors would like to acknowledge helpful discussions with Prof. Xinyuan Zhu of the University of Shanghai for Science and Technology.

References

1 H. Zhang, N. He, B. Wang, B. Ding, B. Jiang, D. Tang and L. Li, *Adv. Mater.*, 2023, **35**, e2300398.
2 R. Yan, X. Zhang, H. Wang, T. Wang, G. Ren, Q. Sun, F. Liang, Y. Zhu, W. Huang and H. D. Yu, *Adv. Mater.*, 2025, **37**, e2418074.
3 R. H. Zhang, X. J. Chen, Z. Z. Wan, M. Y. Yin, L. G. Ma, Z. C. Yang and X. Q. Xiao, *Chem. Eng. J.*, 2024, **502**, 10.
4 J. Min, S. Demchyshyn, J. R. Sempionatto, Y. Song, B. Hailegnaw, C. Xu, Y. Yang, S. Solomon, C. Putz, L. Lehner, J. F. Schwarz, C. Schwarzinger, M. Scharber, E. S. Sani, M. Kaltenbrunner and W. Gao, *Nat. Electron.*, 2023, **6**, 630–641.
5 J.-W. Lee, H.-G. Lee, E. S. Oh, S.-W. Lee, T. N.-L. Phan, S. Li, T.-S. Kim and B. J. Kim, *Joule*, 2024, **8**, 204–223.
6 J. Yin, J. Zhou, S. Fang and W. Guo, *Joule*, 2020, **4**, 1852–1855.
7 Z. Zhang, X. Li, J. Yin, Y. Xu, W. Fei, M. Xue, Q. Wang, J. Zhou and W. Guo, *Nat. Nanotechnol.*, 2018, **13**, 1109–1119.
8 Y. X. Zhang, D. K. Nandakumar and S. C. Tan, *Joule*, 2020, **4**, 2532–2536.
9 X. Wang, F. Lin, X. Wang, S. Fang, J. Tan, W. Chu, R. Rong, J. Yin, Z. Zhang, Y. Liu and W. Guo, *Chem. Soc. Rev.*, 2022, **51**, 4902–4927.
10 F. Zhao, H. H. Cheng, Z. P. Zhang, L. Jiang and L. T. Qu, *Adv. Mater.*, 2015, **27**, 4351–4357.
11 H. H. Cheng, Y. X. Huang, L. T. Qu, Q. L. Cheng, G. Q. Shi and L. Jiang, *Nano Energy*, 2018, **45**, 37–43.
12 T. He, H. Wang, B. Lu, T. Guang, C. Yang, Y. Huang, H. Cheng and L. Qu, *Joule*, 2023, **7**, 935–951.
13 F. Zhao, Y. Liang, H. Cheng, L. Jiang and L. Qu, *Energy Environ. Sci.*, 2016, **9**, 912–916.
14 X. Liu, H. Gao, J. E. Ward, X. Liu, B. Yin, T. Fu, J. Chen, D. R. Lovley and J. Yao, *Nature*, 2020, **578**, 550–554.
15 J. L. Xue, F. Zhao, C. G. Hu, Y. Zhao, H. X. Luo, L. M. Dai and L. T. Qu, *Adv. Funct. Mater.*, 2016, **26**, 8784–8792.
16 S. Lee, J. Eun and S. Jeon, *Nano Energy*, 2020, **68**, 5.
17 S. Yang, L. Zhang, J. Mao, J. Guo, Y. Chai, J. Hao, W. Chen and X. Tao, *Nat. Commun.*, 2024, **15**, 3329.
18 Y. Hu, W. Yang, W. Wei, Z. Sun, B. Wu, K. Li, Y. Li, Q. Zhang, R. Xiao, C. Hou and H. Wang, *Sci. Adv.*, 2024, **10**, eadk4620.
19 Q. Hu, Y. Ma, G. Ren, B. Zhang and S. Zhou, *Sci. Adv.*, 2022, **8**, eabm8047.
20 Y. Huang, H. Cheng, C. Yang, P. Zhang, Q. Liao, H. Yao, G. Shi and L. Qu, *Nat. Commun.*, 2018, **9**, 4166.
21 J. Xu, P. Wang, Z. Bai, H. Cheng, R. Wang, L. Qu and T. Li, *Nat. Rev. Mater.*, 2024, **9**, 722–737.
22 Y. Liang, F. Zhao, Z. Cheng, Y. Deng, Y. Xiao, H. Cheng, P. Zhang, Y. Huang, H. Shao and L. Qu, *Energy Environ. Sci.*, 2018, **11**, 1730–1735.
23 Y. X. Huang, K. Zhou, H. H. Cheng, T. C. He, H. Y. Wang, J. X. Bai, C. Yang, T. L. Guang, H. Z. Yao, F. Li, G. J. Hou, Z. P. Xu and L. T. Qu, *Adv. Funct. Mater.*, 2024, **34**, 11.
24 S. Mandal, S. Roy, A. Mandal, T. Ghoshal, G. Das, A. Singh and D. K. Goswami, *ACS Appl. Electron. Mater.*, 2020, **2**, 780–789.
25 Y. X. Zhang, Z. Yu, H. Qu, S. Guo, J. C. Yang, S. L. Zhang, L. Yang, S. A. Cheng, J. Wang and S. C. Tan, *Adv. Mater.*, 2024, **36**, 9.
26 J. Fang, X. Zhang, P. Duan, Z. Jiang, X. Lu, C. Fu, Y. Zhang, Y. Yao, K. Shang, J. Qin, Y. Liu and T. Yang, *Mater. Horiz.*, 2024, **11**, 1261–1271.
27 D. Ji, J. M. Park, M. S. Oh, T. L. Nguyen, H. Shin, J. S. Kim, D. Kim, H. S. Park and J. Kim, *Nat. Commun.*, 2022, **13**, 3019.
28 X. Wen, Z. Y. Sun, X. Y. Xie, Q. Zhou, H. J. Liu, L. M. Wang, X. H. Qin and S. C. Tan, *Adv. Funct. Mater.*, 2024, **34**, 9.
29 C. Y. Zhang, J. K. Wang, S. Li, X. Q. Zou, H. X. Yin, Y. C. Huang, F. L. Dong, P. Y. Li and Y. T. Song, *Eur. Polym. J.*, 2023, **186**, 12.
30 H. Wang, T. He, X. Hao, Y. Huang, H. Yao, F. Liu, H. Cheng and L. Qu, *Nat. Commun.*, 2022, **13**, 2524.
31 R. B. Zhu, Y. Z. Zhu, F. D. Chen, R. Patterson, Y. Z. Zhou, T. Wan, L. Hu, T. Wu, R. Joshi, M. Y. Li, C. Cazorla, Y. R. Lu, Z. J. Han and D. W. Chu, *Nano Energy*, 2022, **94**, 11.
32 P. Duan, C. Wang, Y. Huang, C. Fu, X. Lu, Y. Zhang, Y. Yao, L. Chen, Q. C. He, L. Qian and T. Yang, *Nat. Commun.*, 2025, **16**, 239.
33 Y. Cheng, T. X. Zhu, Q. H. He, F. Wen, Y. Cheng, J. Y. Huang, Y. K. Lai and H. Q. Li, *Adv. Funct. Mater.*, 2025, **35**, 11.
34 H. Wang, Y. Sun, T. He, Y. Huang, H. Cheng, C. Li, D. Xie, P. Yang, Y. Zhang and L. Qu, *Nat. Nanotechnol.*, 2021, **16**, 811–819.
35 K. S. Moreira, D. Lermen, L. P. dos Santos, F. Galembeck and T. A. L. Burgo, *Energy Environ. Sci.*, 2021, **14**, 353–358.
36 X. Zhang, Z. Dai, J. Chen, X. Chen, X. Lin, S. Yang, K. Wu, Q. Fu and H. Deng, *Energy Environ. Sci.*, 2023, **16**, 3600–3611.
37 W. Duan, B. Shao, Z. Wang, K. Ni, S. Liu, X. Yuan, Y. Wang, B. Sun, X. Zhang and R. Liu, *Energy Environ. Sci.*, 2024, **17**, 3788–3796.
38 L. Wang, H. Wang, C. Wu, J. Bai, T. He, Y. Li, H. Cheng and L. Qu, *Nat. Commun.*, 2024, **15**, 4929.
39 C. Guo, H. Tang, P. Wang, Q. Xu, H. Pan, X. Zhao, F. Fan, T. Li and D. Zhao, *Nat. Commun.*, 2024, **15**, 6100.
40 H. Guo, Q. Luo, D. Liu, X. Li, C. Zhang, X. He, C. Miao, X. Zhang and X. Qin, *Adv. Mater.*, 2024, **36**, e2414285.
41 H. Cheng, Y. Huang, F. Zhao, C. Yang, P. Zhang, L. Jiang, G. Shi and L. Qu, *Energy Environ. Sci.*, 2018, **11**, 2839–2845.
42 P. Li, Y. Hu, W. He, B. Lu, H. Wang, H. Cheng and L. Qu, *Nat. Commun.*, 2023, **14**, 5702.
43 X. W. Yu, M. Zhang, W. J. Yuan and G. Q. Shi, *J. Mater. Chem. A*, 2015, **3**, 6921–6928.
44 R. Q. Liu, S. M. Liang, X. Z. Tang, D. Yan, X. F. Li and Z. Z. Yu, *J. Mater. Chem.*, 2012, **22**, 14160–14167.

45 T. Lu and F. Chen, *J. Comput. Chem.*, 2012, **33**, 580–592.
46 J. Tan, S. Fang, Z. Zhang, J. Yin, L. Li, X. Wang and W. Guo, *Nat. Commun.*, 2022, **13**, 3643.
47 D. Shen, M. Xiao, G. Zou, L. Liu, W. W. Duley and Y. N. Zhou, *Adv. Mater.*, 2018, **30**, e1705925.
48 Z. Sun, X. Wen, L. Wang, J. Yu and X. Qin, *Energy Environ. Sci.*, 2022, **15**, 4584–4591.
49 T. Cai, L. Lan, B. Peng, C. Zhang, S. Dai, C. Zhang, J. Ping and Y. Ying, *Nano Lett.*, 2022, **22**, 6476–6483.
50 M. J. Li, L. Zong, W. Q. Yang, X. K. Li, J. You, X. C. Wu, Z. H. Li and C. X. Li, *Adv. Funct. Mater.*, 2019, **29**, 8.
51 W. Y. He, H. Y. Wang, Y. X. Huang, T. C. He, F. Y. Chi, H. H. Cheng, D. Liu, L. M. Dai and L. T. Qu, *Nano Energy*, 2022, **95**, 9.